Numerical investigation of porosity effect on a PCM's thermal performance in a porous rectangular channel via thermal lattice Boltzmann method

Riheb Mabrouk, Hassane Naji, Hacen Dhahri, Sihem Hammouda, Zohir Younsi

Version of Record: https://www.sciencedirect.com/science/article/pii/S0735193320305200
Manuscript_6a7ec426fd118c94ea8d19cf51a34cea

Numerical investigation of porosity effect on a PCM's thermal performance in a porous rectangular duct via thermal lattice Boltzmann method

Riheb Mabrouk[1], Hassan Naji[2, 1,*] hassane.naji@univ-artois.f, Hacen Dhahri[1], Sihem Hammouda[1], Zohir Younsi[2,3]

[1]École Nationale d'Ingénieurs de Monastir, Université de Monastir, Laboratoire d'Études des Systèmes Thermiques et Énergétiques (LESTE), Rue Ibn Jazza, 5019 Monastir, Tunisia.

[2]Univ. Artois, Univ. Lille, IMT Lille-Douai, Yncréa Hauts de France, Laboratoire Génie Civil & géo-Environnement (ULR 4515), Technoparc Futura, F-62400 Béthune, France.

[3]Yncréa Hauts de France, ULR 4515-LGCgE, F-59000 Lille, France, France.

[*]**Corresponding author.**

Summary

This paper performs a numerical assessment of the porosity effect on heat transfer under forced convection in an open-ended horizontal channel filled with a porous structure and a phase change material (PCM). To take into account forced convection between the solid matrix and the PCM, the dimensionless Darcy-Brinkman-Forchheimer equations and the local thermal non-equilibrium condition are considered. Simulations are achieved via the single relaxation time thermal lattice Boltzmann method using three distribution functions to handle the fluid velocity, and fluid and solid temperatures while translating the computational domain boundary conditions in terms of microscopic distribution functions. The numerical outcomes obtained were used to investigate the porosity effect ($0.5 \le \varepsilon \le 0.9$) on dynamic and thermal fields, entropy generation rate (*Ns*), and Bejan number (*Be*) of the considered system under influence of the Reynolds number (*Re*) during the charging and discharging processes. Based on the findings presented, it can be deduced that, among the various characteristics of metal foam such as conductivity and porosity, the decrease of the latter and the increase in *Re* speeds up the melting under the unsteady, forced and laminar convection. In addition, the overall irreversibility distribution in the proposed system is dominated by the heat transfer irreversibility.

Keywords: Porosity effects; Local thermal non-equilibrium; Phase change material; Unsteady forced convection; Entropy generation rate; Thermal lattice Boltzmann model.

[1] Corresponding author.

✉Univ. Artois, Univ. Lille, Yncréa-HEI, IMT-Douai, Laboratoire Génie Civil &Geo-Environnement (LGCgE - EA 4515) Technoparc Futura, F-62400 Béthune, France

E-mail addresse:*hassane.naji@univ-artois.fr*

ORCID iD
https://orcid.org/0000-0002-5994-7958

Nomenclature

a_{sf}	Specific solid-fluid interfacial area (m^{-1})
Be	Bejan number
Bi	Biot number, $Bi = h_{sf} a_{sf} H^2 / \lambda_s$,
Br	Brinkman number, $Br = Pr.Ec$
c	Lattice speed ($m.s^{-1}$)
C_p	Specific heat capacity at constant pressure ($KJ.Kg^{-1}.K^{-1}$)
c_s	Sound speed ($m.s^{-1}$)
$\overline{\overline{D}}$	Strain tensor (s^{-1})
Da	Darcy number, $Da = K / H^2$
d_f	Ligament diameter (m)
d_p	Average pore diameter (m)
Ec	Eckert number, $Ec = Uo^2 / (C_f . \Delta T_{ref})$
e_i	Discrete velocity in direction *i*
F_ε	Forchheimer form coefficient
F	Body force per unit mass ($N.Kg^{-1}$)
F_{ei}	Discrete body force in direction *i*, ($Kg.m^{-3}.s^{-1}$)
f_i, g_i	Distribution function in direction *i*
f_i^{eq}, g_i^{eq}	Equilibrium distribution function in direction *i*
H	characteristic length scale (m)
h_{sf}	Interfacial heat transfer coefficient ($W.m^{-2}.K^{-1}$)
K	Porous medium permeability (m^2)
K_R	Thermal conductivity ratio, $K_R = \lambda_s / \lambda_f$
L_a	Latent heat ($J.Kg^{-1}$)
Ns	Entropy generation number
p	Pressure (Pa)
P	Dimensionless pressure
Pr	Prandtl number, $Pr = \nu_f / \alpha_f$
Re	Reynolds number, $Re = u_{in} H / \nu_f$
Re_d	Particle Reynolds number, $Re_d = \sqrt{U^2 + V^2}\, d_f / \varepsilon \nu_f$
Rc	Heat capacity ratio, $Rc = (\rho C_p)_s / (\rho C_p)_f$
Ste	Stefan number, $Ste = C_p (T_h - T_m) / L_a$
T	Temperature (K)
T_m	PCM melting temperature, (K)
Θ	Dimensionless temperature
t	Time (s)
u, v	Velocity ($m.s^{-1}$)
U, V	Dimensionless velocity
x, y	Cartesian coordinates (m)
X, Y	Dimensionless coordinates
Greek symbols	

∇	Gradient operator
$\nabla.$	Divergence operator
∇^2	Laplacian operator
Δx	Lattice step
Δt	Time step
$\overline{\overline{\tau}}$	Stress tensor (Pa)
α	Thermal diffusivity ($m^2.s^{-1}$)
ε	Media porosity
η	Energy efficiency
λ	Thermal conductivity ($W.m^{-1}.K^{-1}$)
μ_f	Dynamic fluid viscosity ($Kg.m^{-1}.s^{-1}$)
Γ	PCM's melting fraction
ν	Kinematic viscosity ($m^2.s^{-1}$)
ω	Pore density (PPI)
ψ	Exergy efficiency
ρ	Density ($Kg.m^{-3}$)
$\tilde{t}$	Dimensionless time
τ	Dimensionless relaxation time
w_i	Weight coefficient in direction i
Superscripts/subscripts	
f	Fluid
s	Solid
h	Hot
m	Melting
$\circ$	Initial state
in	Inlet
out	Outlet
Ref	Reference

1. Introduction

Most of research having been carried out on energy storage and thermal management sharply demonstrated that phase change materials (PCMs) constitute one of the best energy storage means and thermal management in latent thermal energy storage systems(LTESS) because of their ability to maintain an almost constant temperature during charging/discharging processes and huge latent heat [1]. To address this problem, new approaches have been suggested which use porous media filled with PCMs, nanoparticles scattered in PCMs, conductive fins and capsules and separate plates [2-5], to name a few. Now, porous media are increasingly used as a proper approach to improve heat transfer. The charging/discharging processes within porous media arises in a broad range of engineering systems and situations in natural setting such as solid-matrix heat exchangers, packed bed-reactors, catalytic and chemical particle beds, soil thermal energy storage, energy solar use, soil melting, pollutants spread, water freezing in soils, paper drying, etc.

Several experimental and numerical researches have been achieved for the natural heat transfer in porous media while being limited to a single phase (without phase change). On the other hand, the problem of heat transfers by forced convection in porous media filled with PCM has hardly been dealt. Note that modelling and simulating such a problem remains a daunting task due to the porous metallic medium complexity and the phase change process taking place.

Initially, research on these problems was carried out by invoking the hypothesis of local thermal equilibrium (LTE). However, it turned out that such a hypothesis could collapse in favor of the local thermal imbalance (LTNE) then requiring the use of two energy equations (called the LTNE models or two-phase models), one for each phase (solid and liquid). Such models can detect LTE zones in forced convection. For metal-foams fully filled channel, Lee and Vafai [6] and Xu et al. [7] strongly advise to use such a model. In addition, many studies have confirmed that such an assumption can manage these problems at the representative elementary volume (REV) scale.

Among the key parameters making porous media complex is the fraction of pore from which the volume proportion between the metal foam ligament and the PCM can be determined. This is the so-called porosity. Such a parameter may or may not further the heat transfer and the melting (charging) and/or solidifying (discharging) processes throughout the medium considered. Although the porosity is in the range 0.8-0.9 for metallic foams, we are rather considering the range 0.5-0.9 herein. This range could be extended to low porosities (0.5 - 0.7) since these are linked to large volume fractions, thereby promoting the heat transfer.

It should be noted that the interest of forced convection heat transfer in porous media stems from engineering applications [8, 9], to cite a few. To save energy, Xu et al. [10] have investigated forced convective heat transfer in a metallic foam filled-parallel channel by providing ranges of foam parameters. Mesalhy et al. [11] stated that decreasing the porosity of the matrix increases the melting rate, while damping the convection motion inside a geometry filled with high thermal conductivity porous matrix saturated with PCM due to the matrix permeability decrease. Yang et al. [12] suggested to use a metal foam with linearly changed porosity, and the numerical results revealed that this structure could enhance the PCM phase change process.

While past or present numerical simulations often come from traditional approaches such as finite differences or finite element methods, more recently, the lattice Boltzmann method (LBM), arising from a different perspective based on kinetic theory, has shown an outstanding potential for tackling these complex fluid problems with convective heat transfer in porous media with or without phase change [13-16]. In particular, it is obtained through

Boltzmann equation discretization, which advances particle distribution functions via a shift streaming process along the lattice directions, which is followed by a local collision process modelled as a relaxation process to certain equilibria. In addition, its ease of representing boundary conditions based on particles, its parallelization capabilities, and its numerical stability have made it an increasingly adopted technique for numerically handling complex problems.

Hereinafter, a brief review of works that use the LBM to simulate heat transfer under forced convection through porous media including or not a phase change material. Tao et al. [17] achieved an LBM simulation to study the latent heat storage (LHS) performance of metal foams filled with paraffin. They found out that the porosity decreasing improved the heat storage rate while reducing the heat storage density. Jiaung et al. [18] performed LBM simulation to settle the phase change problem generated by thermal conduction via the enthalpy formulation while achieving different thermal diffusivities in the separate phases/zones. He et al [19] carried out a full review on the LBM approach to numerically handle single-phase heat transfer and solid-liquid phase change in porous media. Gao et al [20] applied the LBM to simulate transient melting heat transfer of phase change material in porous media coupled with conduction fins at the REV scale. They have demonstrated that the melting heat transfer can be further improved by fins addition. The PCM (wax) melting behavior in metallic foams at the REV scale with experimental support has been numerically examined by Chen et al. [21]. They pointed out that the PCM heat transfer during the melting is enhanced using a dual population LBM.

Investigation of unsteady forced convective melting in a porous rectangular duct saturated with a PCM remain scarce in the literature. Thereby, in our view, this challenge is an open research topic that may require further studies. So, the main purpose herein is to study numerically the porosity effect of a matrix on the phase change in charging and discharging cases. These simulations have been achieved using the enthalpy method with the single relaxation time (SRT)-LBM.

The current investigation is split into six sections. In Section 2, the problem physics regarding porous flow, temperature and entropy generation, including the normalization approach and boundary conditions, is provided. In Section 3, the computational method for fluid flow and heat transfer along with the LB boundary conditions are outlined. In Section 4, grid check and code validation study are examined. Section 5 presents and comments on the outcomes obtained. Finally, Section 6 draws the main conclusions regarding the present results.

2. Problem's physics and formulation

2.1. Problem description

The two-dimensional (2D) open-ended channel filled with paraffin-saturated metal foam is the interest domain for this work, as schematically illustrated in Fig. 1. The channel length is L and it height is H. As seen, both upper and lower channel walls are thermally adiabatic, impermeable and non-slip. The fluid flow enters the channel with a constant hot temperature T_h and at a uniform initial velocity U_0 and leaves it at a constant cold temperature T_c for the charging process, to return with to perform the discharging process. The outlet conditions are supposed fully developed so that the problem is 2D. For the present problem, the Reynolds number $Re = (U_0 H / \nu_f)$) range is of $200 \le Re \le 400$.

Note that, to initiate the first process (charging), the inlet temperature is set to T_h $(> T_m)$ so that the PCM can start to melt.

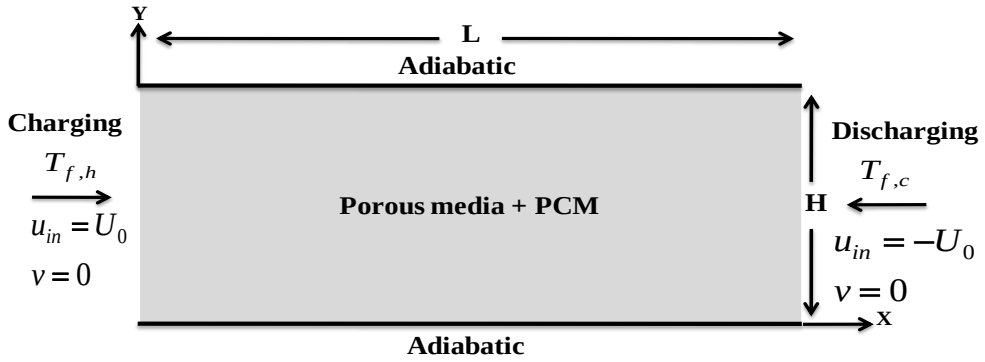

Fig. 1. Schematic view of the physical model along with boundary conditions (charging and discharging cases).

2.2. Assumptions drawn up

The assumptions on which the governing equations are based are as follows: The flow under consideration is unsteady forced convective. The fluid flow and the liquid paraffin are assumed to be laminar, incompressible. Viscous dissipation is considered while natural convection and interfacial radiation are neglected. In addition, the LTNE condition stands between solid and fluid phases. The thermo-physical properties of porous matrix (copper) as well as of the PCM (paraffin) remain constant with respect to the temperature, homogeneous and isotropic. Note that due to the incorporated fusion/solidification phenomena, the charge/discharge processes to be studied are basically unsteady. Moreover, in REV approach, the porous medium effect is reflected through the governing equations homogenization. Thereby, the flow is modeled by the DBF equations in the porous matrix, and by the Navier-Stokes equations in the fluid domain. For more details, one can refer, e.g., to Nield and Bejan [9].

2.3. Macroscopic equations for porous flow and heat transfer

Given the assumptions up-mentioned, the transient macroscopic governing equations at the REV scale can be recast under the following canonical dimensional form [9, 22, 23]:

• Porous flow's equations

$$\nabla \cdot \vec{U} = 0 \tag{1}$$

$$\frac{\partial \vec{U}}{\partial t} + \left(\vec{U}.\nabla\right)\left(\varepsilon^{-1}\vec{U}\right) = -\nabla\left(\varepsilon P\right) + \nu_f \nabla^2 \vec{U} + \varepsilon.\vec{F} \tag{2}$$

• Thermal equations for the PCM and metal skeleton

$$\varepsilon\left(\rho C_p\right)_f \left(\frac{\partial T_f}{\partial t} + u.\nabla T_f\right) = \nabla.\left(\lambda_{eff,f} \nabla T_f\right) + h_{sf} a_{sf} \left(T_s - T_f\right) - \varepsilon \rho_f L_a \frac{\partial \Gamma}{\partial t} + \Phi \tag{3}$$

$$\left(1-\varepsilon\right)\left(\rho C_p\right)_s \frac{\partial T_s}{\partial t} = \nabla.\left(\lambda_{eff,s} \nabla T_s\right) + h_{sf} a_{sf} \left(T_f - T_s\right) \tag{4}$$

where $\vec{U}$, P, T_f, T_s, ε, ρ, ν_f, C_p and λ_{eff} are the velocity vector filed, pressure, fluid and porous medium temperatures, copper porosity, density, kinematic viscosity of PCM, thermal capacity and the equivalent thermal conductivity, respectively. Subscripts f and s point out the fluid and solid phases, respectively. Also, Γ, L_a, a_{sf} and h_{sf} are the liquid fraction in pore space, the PCM latent heat, specific surface area of the porous matrix, and the local interfacial heat transfer coefficient between copper and paraffin, respectively.

Note that $\vec{F}$ (Eq. (2)) denotes the total body force due to the presence of porous media which can be expressed as [24]:

$$\vec{F} = -\left(\frac{\nu_f}{K} + \frac{F_\varepsilon}{\sqrt{K}}\left|\vec{U}\right|\right)\vec{U} \tag{5}$$

K and F_ε being the permeability and the Forchheimer's form coefficient which, in general, are not universal. Here, they are expressed as [17]:

$$F_\varepsilon = 2.12\times10^{-3}(1-\varepsilon)^{-0.132}\left(\frac{d_p}{d_f}\right)^{+1.63} \tag{6}$$

$$K = \varepsilon^3 d_p^2 \left(150\left(1-\varepsilon\right)^2\right)^{-1} \tag{7}$$

Note that all the coefficients involved above are empirical since they depend mainly on the metallic foam geometry, the solid and the fluid thermal properties, and on the flow rate.

With the LTNE model adopted here, the solid-fluid interfacial specific area (a_{sf}) and the local heat transfer coefficient (h_{sf}) must be predicted. So, they were computed from the following Zukauskas correlations [25]:

$$a_{sf} = 3\pi d_f (1-e^{-(1-\varepsilon)/0.004})/(0.59 d_p)^2 \tag{8}$$

$$h_{sf} = \begin{cases} 0.76.Re_d^{0.4}\, Pr^{0.37}\, \frac{\lambda_f}{d_f} & \\ 0.52.Re_d^{0.5}\, Pr^{0.37}\, \frac{\lambda_f}{d_f} & for \\ 0.26.Re_d^{0.6}\, Pr^{0.37}\, \frac{\lambda_f}{d_f} & \end{cases} \begin{matrix} 1 \le Re_d \le 40 \\ 140 \le Re_d \le 10^3 \\ 10^3 \le Re_d \le 2.10^5 \end{matrix} \quad (9)$$

with $d_f = 1.18 \times \left((1-\varepsilon)/3\pi\right)^{1/2} d_p$ *and* $d_p / H = 0,0135$ [24].

Using the enthalpy method, the liquid fraction Γ appearing in Eq. (3) could be computed as [26]:

$$\Gamma = \begin{cases} 0 & T \prec (T_m - \Delta T) \\ \left(T - T_m + \Delta T\right)/2\Delta T & if \quad (T_m - \Delta T) \le T \le (T_m + \Delta T) \\ 1 & T \succ (T_m + \Delta T) \end{cases} \quad (10)$$

Recall, that both the PCM and solid temperatures are at equilibrium at initial temperature and that, at the channel inlet, the temperature is raised to allow the PCM to start melting.

In Eq. (3), the last term is associated to the viscous heat dissipation within the PCM which can be calculated as follows [27]

$$\Phi = \varepsilon \left\{ \frac{\mu}{K} + \frac{F_\varepsilon}{\sqrt{K}} |u| \right\} |u|^2 + \mu \left\{ 2 \left[\left(\frac{\partial u}{\partial x} \right)^2 + \left(\frac{\partial v}{\partial y} \right)^2 \right] + \left(\frac{\partial u}{\partial y} + \frac{\partial v}{\partial x} \right)^2 \right\} \quad (11)$$

The associated boundary conditions (BCs) and initial condition (IC) needful to complete the problem formulation are the following:

- $u = u_{in}$; $v = 0$; $T_f = T_h$, at $x = 0$ and $0 \le y \le H$ (left boundary);
- $\nabla_x u = 0$; $v = 0$; $T_f = T_c$ at $x = L$ and $0 \le y \le H$ (right boundary);
- $u = 0$; $v = 0$ (no-slip condition) and $\nabla_y T_f = \nabla_y T_s = 0$ (perfect-insulated) at $0 \le x \le L$ and $y = H$ (upper boundary);
- $u = 0$; $v = 0$ (no-slip condition) and $\nabla_y T_f = \nabla_y T_s = 0$ (perfect-insulated) at $0 \le X \le L$ and $y = 0$ (lower boundary);
- $u = 0$; $v = 0$ and $T_f = T_c = T_0$ at $t = 0$ for $0 \le x \le L$ and $0 \le y \le H$

Note that, during discharging period, fluid flow take the inverse way with $u = -u_{in}$ (see Fig. 1).

2.4. Normalization and key parameters

The key dimensionless variables and parameters are introduced as:

$$\left(X, Y\right) = \left(x, y\right)/H \ , \ U = u/U_0 \ , \ P = p/\rho U_0^2 \ , \ \tilde{t} = tU_0/H \ , \ \Theta = \left(T - T_c\right)/\left(T_h - T_c\right) \ , \ \Delta T_{ref} = T_h - T_c \ ,$$
$$Da = K/H^2, \ \Pr = \nu_f / \alpha_f, \ Re = U_{in} H / \nu_f, \ Rc = (\rho C_p)_s / (\rho C_p)_f, \ Kr = \lambda_s / \lambda_f, \ Bi = h_{sf} a_{sf} H^2 / \lambda_s,$$
$$Ste = C_{pf}(T_h - T_m)/La, \ Ec = U_0^2 / \left(C_f \Delta T_{ref}\right) \quad (12)$$

Then, Eqs. (1) - (4) are rewritten in dimensionless form as [9, 23, 28, 29]

$$\nabla \cdot \vec{U} = 0 \quad (13)$$

$$\frac{\partial U}{\partial \tilde{t}}+\left(\vec{U}.\nabla\right)\left(\varepsilon^{-1}\vec{U}\right)=-\nabla\left(\varepsilon P\right)+\frac{1}{Re}\nabla^2\vec{U}+\varepsilon\vec{\vec{F}} \tag{14}$$

$$\frac{\partial\Theta_f}{\partial\tilde{t}}+U.\nabla\Theta_f=\frac{1}{Re.Pr}\nabla.\left(\frac{\lambda_{eff,f}}{\lambda_f}\nabla\frac{\Theta_f}{\varepsilon}\right)+Kr.\frac{Bi}{Re.Pr}\left(\frac{\Theta_s-\Theta_f}{\varepsilon}\right)-\frac{1}{Ste}\frac{\partial\Gamma}{\partial\tilde{t}}+\tilde{\Phi} \tag{15}$$

$$\frac{\partial\Theta_s}{\partial\tilde{t}}=\frac{Kr}{Rc}\frac{1}{Re.Pr}\nabla.\left(\frac{\lambda_{eff,s}}{\lambda_s}\nabla\frac{\Theta_s}{1-\varepsilon}\right)-\frac{Kr}{Rc}.\frac{Bi}{Re.Pr}\left(\frac{\Theta_s-\Theta_f}{1-\varepsilon}\right) \tag{16}$$

where $\vec{\vec{F}}=-\left(\frac{1}{Re\,Da}+\frac{F_\varepsilon}{\sqrt{Da}}\left\|\vec{U}\right\|\right)\vec{U}$ (17)

$$\tilde{\Phi}=\varepsilon.Ec\left\{\frac{1}{Da.Re}+\frac{F_\varepsilon}{\sqrt{Da}}\left\|\vec{U}\right\|\right\}\left\|\vec{U}\right\|^2+\frac{Ec}{Re}\left\{2\left[\left(\frac{\partial U}{\partial X}\right)^2+\left(\frac{\partial V}{\partial Y}\right)^2\right]+\left(\frac{\partial U}{\partial Y}+\frac{\partial V}{\partial X}\right)^2\right\} \tag{18}$$

It is noteworthy that, in the model considered, the thermal conductivity ratio is $Kr=10^3$ (*fixed value*) and the interfacial heat transfer (paraffin/metallic foam) is drawn from the Biot number (Bi = 0.1). Such a number is a key parameter to secure the LTE and/or LTNE assumptions in porous media. Previous studies dealt with LTNE and LTE conditions [29, 30, 31]. From these studies, it appeared that, to satisfy the LTNE condition, Bi must be low ($Bi\le 0.1$) while filling the condition $Bi/Kr\ll 1$, which takes place in our study.

For the charging process, the associated dimensionless BCs and IC are translated as:

- $U=1$; $V=0$; $\Theta_{f,h}=1$, at $X=0$ and $0\le Y\le 1$;
- $\nabla_X U=0$; $V=0$; $\Theta_{f,c}=0$ at $X=L/H$ and $0\le Y\le 1$;
- $U=0$; $V=0$ and $\nabla_y\Theta_{f,h}=\nabla_y\Theta_{f,s}=0$ at $0\le X\le L/H$ and $Y=1$;
- $U=0$; $V=0$ and $\nabla_y\Theta_{f,h}=\nabla_y\Theta_{f,s}=0$ at $0\le X\le L/H$ and $Y=0$;
- $U=0$; $V=0$ and $\Theta_f=0=\Theta_s$ at $\tilde{t}=0$ for $0\le X\le L/H$ and $0\le Y\le 1$.

Note that, during discharging process, $U=-1$.

2.5. Entropy generation and Bejan number

As the entropy generation is given rise by the irreversibilities within the system by heat transfer (HTI) and by fluid friction (FFI), the local entropy generation rate under LTNE condition can be written as [30, 32]

$$Ns=\underbrace{\frac{k_f}{T_f^2}\left(\left\|\nabla T_f\right\|\right)^2+\frac{\overline{\overline{D}}:\overline{\tau}}{T_f}+\frac{1}{T_f}\left(\frac{\varepsilon\mu}{K}+\frac{\varepsilon F_\varepsilon}{\sqrt{K}}\left\|\vec{U}\right\|\right)\left\|\vec{U}\right\|^2+\frac{a_{sf}h_{sf}}{T_f}(T_s-T_f)}_{Ns_f}$$
$$+\underbrace{\frac{k_s}{T_s^2}\left(\left\|\nabla T_s\right\|\right)^2-\frac{a_{sf}h_{sf}}{T_s}(T_s-T_f)}_{Ns_s} \tag{19}$$

where $\overline{\overline{D}}:\overline{\tau}=\mu\left[2\left(\left(\frac{\partial u}{\partial x}\right)^2+\left(\frac{\partial v}{\partial x}\right)^2\right)+\left(\frac{\partial u}{\partial y}+\frac{\partial v}{\partial x}\right)^2\right]$ (20)

$\overline{\overline{D}}$ and $\overline{\tau}$ being the strain and stress tensors, and Ns_f and Ns_s are the dimensionless entropy generation for the fluid and solid phases, respectively.

The entropy generation rate Ns can be rewritten in terms of HTI and FFI as

$$Ns=\underbrace{\frac{k_f}{T_f^2}\left(\left\|\nabla T_f\right\|\right)^2+\frac{k_s}{T_s^2}\left(\left\|\nabla T_s\right\|\right)^2+\frac{a_{sf}h_{sf}}{T_fT_s}\left(T_s-T_f\right)^2}_{HTI}+\frac{1}{T_f}\underbrace{\left(\overline{\overline{D}}:\overline{\tau}+(\frac{\varepsilon\mu}{K}+\frac{\varepsilon F_\varepsilon}{\sqrt{K}}\left\|\vec{U}\right\|)\left\|\vec{U}\right\|^2\right)}_{FFI} \quad (21)$$

The average entropy generation rate through the entire channel per unit of volume can be calculated as [27]

$$Ns_{ave}=\frac{1}{S}\int_S Nsdxdy \quad (22)$$

It is worth pointing out that the origin of irreversibility can also be assessed via the Bejan number (Be) which ranges from 0 to 1 and whose expression is [27]

$$Be=HTI/\left(HTI+FFI\right) \quad (23)$$

Its average value can be computed as [27]

$$Be_{ave}=\frac{1}{S}\int_S Bedxdy \quad (24)$$

3. Lattice Boltzmann model

The lattice Boltzmann method (LBM) is a mesoscale model that can cope with the aforementioned governing equations (see Section 2.3). It recently achieved substantial success in solving even complex fluid flows. Briefly, such an approach handles a straightforward evolution of fluid particle clusters using a density distribution function (DDF) $f\left(x,t\right)$ which portrays the particle evolution at time *t* positioned at *x* and having a velocity e_i allowing it to propagate towards neighboring sites within a regular lattice. The particles propagate towards their neighboring lattice points and redistribute their momenta according to two main sub-steps during a time step, viz., streaming and collision processes. To the best of our knowledge, the LBM can handle different physical phenomena in porous media with various and complex pores geometry using two main categories, namely (1) the pore scale approach [17] which is limited in terms of geometry and the computational domain size, and (2) the REV approach [33] which is frequently applied. In the first class, porous media' effect could be reflected via the solid porous matrix incorporation with complex geometry in the computational domain, while in the second class, this effect could be reflected through

governing equations homogenization, the so-called volume averaging approach. Yet, none of these categories considered the phase change phenomenon. In addition, the forced convection in porous domain is often handled under local thermal equilibrium condition. To cope with the present study under LTNE condition, the REV-scale LBM has been applied with three DDF (TDDF) for dynamic and thermal fields of PCM and solid foam [34].

3.1. Lattice Boltzmann equation (LBE) for fluid flow

As previously itemized, the flow governing equations (1) - (2) are shaped through the modified BGK (Bhatnagar-Gross-Krook)-LBE. Thereby, under the SRT approximation, the velocity is obtained via the DDF f_i [35] as

$$\underbrace{f_i\left(x+e_i\delta t,t+e_i\delta t\right)-f_i\left(x,t\right)}_{streamin g}=-\delta t\omega_i\underbrace{\left[f_i\left(x,t\right)-f_i^{eq}\left(x,t\right)\right]}_{collision}+\delta t.\underbrace{F_{e_i}}_{force\ term} \tag{25}$$

here, $\omega_i\,(=1/\tau_v)$ is the single relaxation collision frequency, calculating from the dimensionless relaxation time $\tau_v\,(=3\nu+0.5)$; δt is the time increment, and $f_i^{eq}\left(x,t\right)$ is the equilibrium fluid distribution function (EFDF) which can be expressed, for the D2Q9 (2D and 9 lattice-velocities) model (Fig. 2), as

$$f_i^{eq}=\rho w_i\left(1+\frac{e_iu}{c_s^2}+\frac{uu:\left(e_ie_i-c_s^2I\right)}{2c_s^4\varepsilon}\right) \tag{26}$$

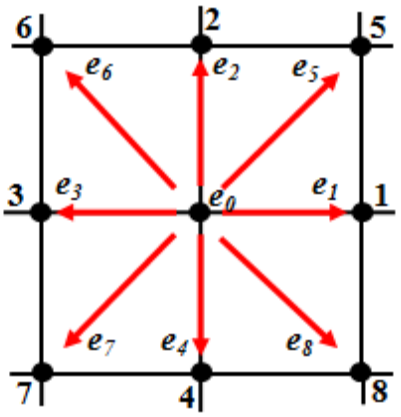

Fig. 2. D2Q9 stencil (2D and 9-lattice velocities)

where, the discrete velocity e_i in direction i, is given as

$$e_i=\begin{cases}0\vec{i}+0\vec{j}, & i=0\\ c\left(\cos\left((i-1)\pi/2\right)\vec{i}+\sin\left((i-1)\pi/2\right)\vec{j}\right), & i=1,2,3,4\\ \sqrt{2}c\left[\cos\left((2i-9)\pi/4\right)\vec{i}+\sin\left((2i-9)\pi/4\right)\vec{j}\right], & i=5,6,7,8\end{cases} \tag{27}$$

where $c\,(=\delta x/\delta t)$ is the lattice velocity set at 1 since the mesh adopted is uniform with $\delta x=\delta t$, and weighting factor (w_i) is set as: $w_0=4/9$, $w_{1,4}=1/9$ and $w_{5,8}=1/36$. Here,

c_s $(=e_i/\sqrt{3})$ is the sound speed and I is the unit tensor. In the REV scale, the porous media effect on the flow (see Eq. (25)) is modelled as [36]

$$F_{ei} = F\left(e_i - u\right)^2 f_i^{eq} / RT_0 \tag{28}$$

Using the mass and momentum conservation at each lattice node, the macroscopic density and velocity are obtained, respectively, via the relationships:

$$\rho = \sum_i f_i\,, \qquad u = \sum_i f_i e_i / \rho + \delta t F_{e_i} / 2 \tag{29}$$

From the mathematical programming standpoint, Eq. (25) is implemented via the following two sequential steps (streaming (Eq. (30) and collision (Eq. (31)):

$$f_i^*\left(x,t\right) = f_i\left(x,t\right) - \delta t\omega_i\left(f_i\left(x,t\right) - f_i^{eq}\left(x,t\right)\right) + \delta t F_{e_i} \tag{30}$$

$$f_i\left(x + e_i\delta t, t + e_i\delta t\right) = f_i^*\left(x,t\right) \tag{31}$$

In these equations, $f_i^*\left(x,t\right)$ is the post-collision distribution function. Note that the collision step, whose relaxation model can be tuned to represent a variety of flow physics, obviously has a predominant role in the method numerical stability.

3.2. LBE for heat transfer

To obtain the temperature field, two thermal distribution functions $g_{i,f;s}$ are used to solve the energy Eqs. (3) - (4), respectively. For PCM-solid matrix, the discretized SRT-TLBM equations are given as [17, 24]:

$$\begin{aligned} g_{f,i}\left(x + e_i\delta t, t + \delta t\right) - g_{f,i}\left(x,t\right) = -\omega_{T,f}\left(g_{f,i}\left(x,t\right) - g_{f,i}^{eq}\left(x,t\right)\right) + \left(1 + \delta t\partial_t / 2\right)\delta t Sr_{i,f} \\ + \delta t f_i\left(x,t\right) q_i \end{aligned} \tag{32}$$

$$g_{s,i}\left(x + e_i\delta t, t + \delta t\right) - g_{s,i}\left(x,t\right) = -\omega_{T,s}\left(g_{s,i}\left(x,t\right) - g_{s,i}^{eq}\left(x,t\right)\right) + \left(1 + \delta t\partial_t / 2\right)\delta t Sr_{i,s} \tag{33}$$

where, the subscripts f and s point out the fluid and solid phases, $\omega_{T,f;s}\,(=1/\tau_{T,f;s})$ are single relaxation collision frequencies which can be computed via the dimensionless relaxation times ($\tau_{T,f;s}$) expressions as follows [24, 37]:

$$\tau_{T,f} = 3\alpha_{e,f}/(\delta t c^2) + 0.5 \quad with \quad \alpha_{e,f} = k_{e,f}/\left(\varepsilon(\rho C_p)_f\right) \tag{34}$$

$$\tau_{T,s} = 3\alpha_{e,s}/(\delta t c^2) + 0.5 \quad with \quad \alpha_{e,s} = k_{e,s}/\left((1-\varepsilon)(\rho C_p)_s\right) \tag{35}$$

$\alpha_{e,f}$ and $\alpha_{e,s}$ being the effective diffusivities of the PCM and the solid matrix, respectively.

The equilibrium temperature distribution function (ETDF) $g_{i,f;s}^{eq}$ can be computed for as follows:

$$g_{f,i}^{eq} = w_i T_f\left(1 + e_i u/(\varepsilon c_s^2)\right) \text{ and } g_{s,i}^{eq} = w_i T_s \tag{36}$$

As for source terms $Sr_{i,f;s}$ appearing in Eqs. (32) - (33), they can be given by, respectively [24, 37]:

$$Sr_{i,f} = w_i\left(La\left(\frac{\gamma(t+\delta t)-\gamma(t)}{\delta t}\right)/C_{p,f} + h(T_s - T_f)/\left(\varepsilon(\rho C_p)_f\right)\right) \tag{37}$$

$$Sr_{i,s} = w_i\left(\frac{h(T_s - T_f)}{(1-\varepsilon)(\rho C_p)_s}\right) \tag{38}$$

As stated by Shi et al. [38], the quantity q_i (see the last source term of Eq. (32)) appoints the viscous heat dissipation, which can be given by

$$q_i = -\left(f_i - f_i^{eq}\right)(e_i - u)(e_i - u) : \Delta u \tag{39}$$

Finally, the fluid and solid macroscopic temperatures are defined respectively as:

$$T_f = \sum g_{fi}\,, \qquad T_s = \sum g_{si} \tag{40}$$

3.3 LBM boundary conditions' implementation

As with other methods, properly implemented boundary conditions (BCs) are crucial for physical significance, accuracy and numerical stability when dealing with LBM simulations. In the present study, the bounce-back boundary scheme is adopted to express the no-slip velocity conditions. To better translate the BCs into LBM, the particles located inside the computation domain, at its entry and at its exit, and on its solid boundaries, are firstly illustrated in Fig. 3, which exhibits the domain boundaries layout and notation along with the streaming velocities (D2Q9) for both the momentum and energy transport equations, with their unknowns.

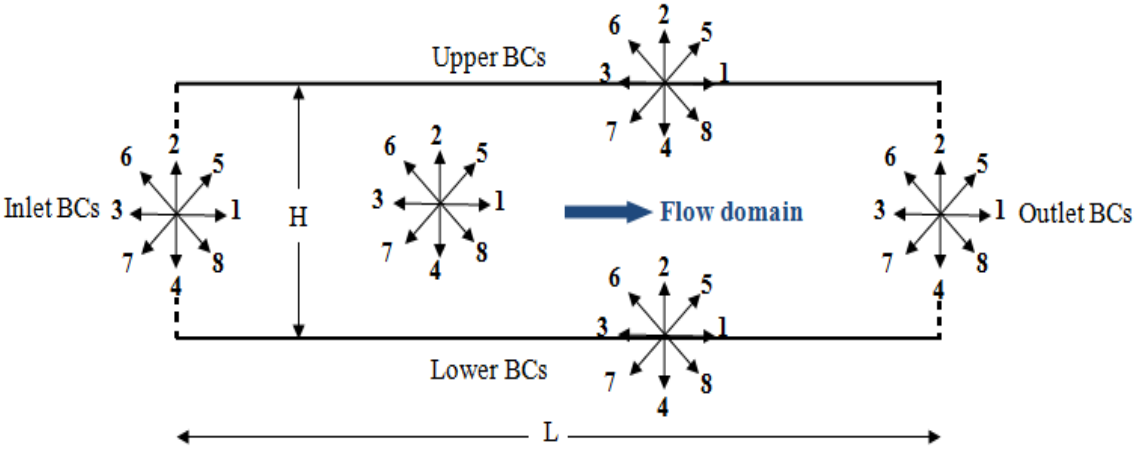

Fig. 3. D2Q9 velocity and temperature lattice layout within and at domain boundaries.

Here, the LBM BCs deal with microscopic distribution functions f and g. Note that, in LBM framework, the DDFs' values within the computational domain are obviously unknown.

At each node, the unknown distribution functions are expressed in terms of those that are known.

• Boundary conditions for velocity field

▪ *At the inlet (west)*

The velocity is specified at the input and is dealt as a Dirichlet condition using the approaches coming from Refs. [39 - 41] for the unknowns. So, due to the D2Q9 choice and referring to Fig. 3, the density ρ_{in} as well as f_1, f_5, f_8, at the domain inlet, are computed using the following relationships:

$$\begin{aligned} &\rho_{in} = \left(f_0 + f_2 + f_4 + 2\left(f_3 + f_6 + f_7 \right) \right) / \left(1 - u_{in} \right) \\ &f_1 = f_3 + 2\rho_{in} u_{in} / 3; \quad f_5 = f_7 + \rho_{in} u_{in} / 6; \quad f_8 = f_6 + \rho_{in} u_{in} / 6 \end{aligned} \tag{41}$$

▪ *At the upper and lower insulated boundaries*

Imposing $u = 0$ implies that an incoming particle towards the solid boundary bounces in the flow domain. Consequently, for every wall, the non-slip boundary condition can, respectively, be set by [42]:

$$f_{i,n} = f_{i(opposite),n} \quad with \;\; 0 \le i \le 8 \tag{42}$$

Note that it is f_4, f_7, f_8 (at the upper wall) and f_2, f_5, f_6 (at lower wall), which are the unknowns.

▪ *At outlet (east)*

Unlike the channel inlet, the exit velocity is unknown. So, unknown DDFs can be written as

$$f_{3,n-1} = f_{3,n}; \qquad f_{7,n-1} = f_{7,n}; \qquad f_{6,n-1} = f_{6,n} \tag{43}$$

where *n-1* and *n* indicate nodes put inside and outside the channel, respectively.

• Thermal boundary conditions

Note that, in our case, the temperatures of the fluid and the solid relate to the same boundary.

▪ *At inlet*

Recall that, at the channel inlet, the fluid enters with a hot temperature $T_w = \Theta_h = 1$ (see Section 2.4). Thereby, the DDF g can be given by:

$$g_1 = T_w(w_1 + w_3) - g_3; \qquad g_5 = T_w(w_5 + w_7) - g_7; \qquad g_8 = T_w\left(w_8 + w_6 \right) - g_6 \tag{44}$$

▪ *At upper and lower insulated boundaries*

Due to the non-slip condition at solid walls, the on-grid bounce-back boundary condition has been adopted on the adiabatic lower and upper walls of the channel. Thereby, the DDFs equations can be set as [42]

At the upper:

$$g_{8,m} = g_{8,m-1}; \qquad g_{4,m} = g_{4,m-1}; \qquad g_{7,m} = g_{7,m-1} \tag{45}$$

where *m-1* and *m* indicate two adjacent nodes in the *y*-direction.

At the lower:

Similarly, the temperature boundary conditions on the lower wall can be written in terms of DDFs (g_2, g_5 and g_6). These are:

$$g_{6,0} = g_{6,1} \qquad g_{2,0} = g_{2,1}; \qquad g_{5,0} = g_{5,1}; \tag{46}$$

▪ *At outlet*

At the channel outlet, the temperature DDFs ((g_3, g_6 and g_7) are set as

$$g_7 = -g_5; \qquad g_3 = -g_1; \qquad g_6 = -g_8 \tag{47}$$

It is this boundary conditions set that has been implemented in the SRT-TLBM for the velocity and temperature fields.

4. Grid check and model validation

4.1. Grid check

Numerical outcomes need to be independent for the grid used. Hence, the grid study is performed before validating. Thereby, simulations have been performed for a *Re* number of 200 using several (six) grids, viz. 320×80, 400×100, 460×115, 480×120, 500×125 and 550×130. Fig. 4 shows dimensionless solid temperature (Θ_s) profiles vs. the transverse distance X at $Y = 0.5$ for $Pr = 50, Bi = 0.1, Ste = 1, Kr = 10^{+3}, Rc = 1, Ec = 5$ and $\varepsilon = 0.5$. As shown the difference between the first and second grid (320×80 and 400×100) is 3.4% that is reduced to 2.1% compared with third grid (460×115). As seen, the last three grids are closer to each other exhibiting a maximum discrepancy of 0.6%, thereby indicating that the solution becomes independent of grid size at 480x120 for the case dealt. This size is a best trade-off between accuracy and computation time. So, from now on, it is adopted for subsequent computations.

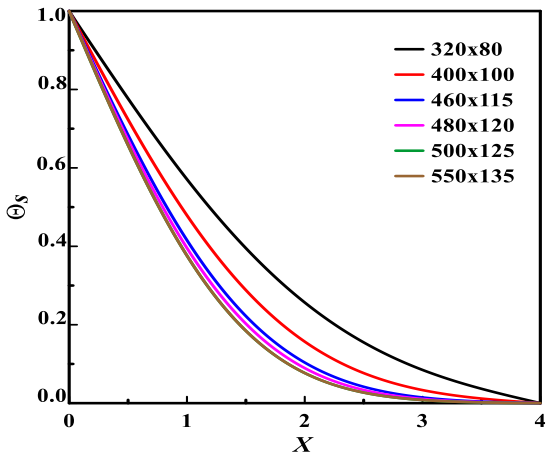

Fig. 4. Mesh independency test of dimensionless solid temperature (Θ_s) profiles for $Re = 200$ at Y=0.5 with $Pr = 50, Bi = 0.1, Ste = 1, Kr = 10^{+3}, Rc = 1, Ec = 5$ and $\varepsilon = 0.5$.

4.2. Model validation

Previously, the mathematical model and the numerical scheme must to be validated with one or more relevant limiting cases available in the literature. To demonstrate this validity, Fig. 5 shows a comparison of the predicted *U*-velocity profiles from the present study with those of Kim et al. for [43] at different *Da* numbers. Likewise, Fig. 6 presents the comparison of the intensity LTNE ($\Theta_s - \Theta_f$) obtained by TLBM with results of Abdedou et al. [31] at two axial positions for $Da = 10^{-4}, Bi = 10^{-2}, Re = 10^{+2} = Rq$ and $Kr = 1$. A close look at these figures shows that all our outcomes exhibit shows a good agreement.

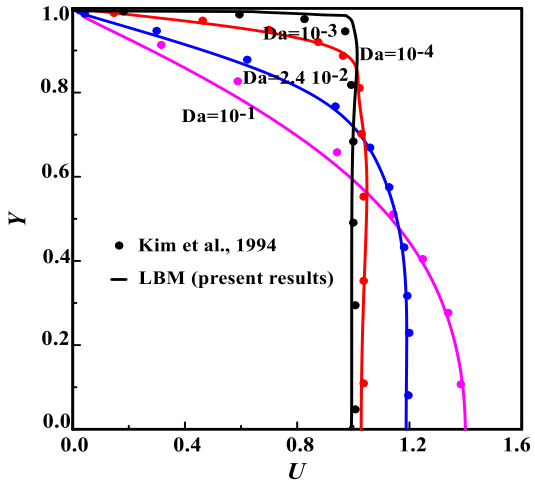

Fig. 5. Darcy number's effect on velocity profiles vs. dimensionless transverse distance at X = 0.5 for *Re* = 50 and *Pr* = 0.7.

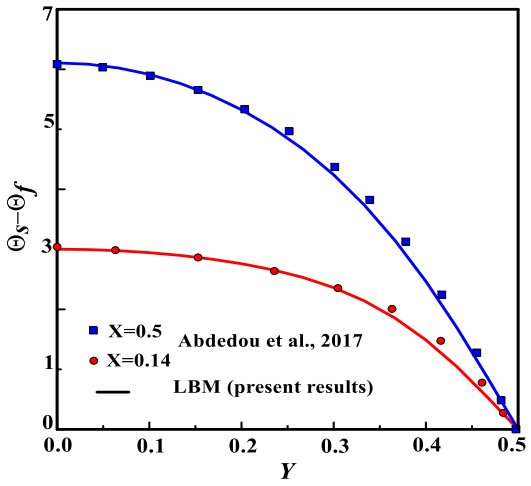

Fig. 6. LTNE intensity $(\Theta_s - \Theta_f)$ vs. dimensionless distance Y at two axial positions for $Da = 10^{-4}, Bi = 10^{-2}, Re = 10^{2} = Rq$ and $Kr = 1$.

To further support our prior validation, Fig. 7 depicts fluid (Θ_f) and solid (Θ_s) temperature evolutions along Y = 0.5 for $Nu_i = 0, Da = 10^{-2}, Pr = 50, Ra = 10^{6}, Ste = 1$, and reveals that they agree well with those predicted by Krishnan et al. [44], thereby confirming our in-house code reliability and the model validity implemented.

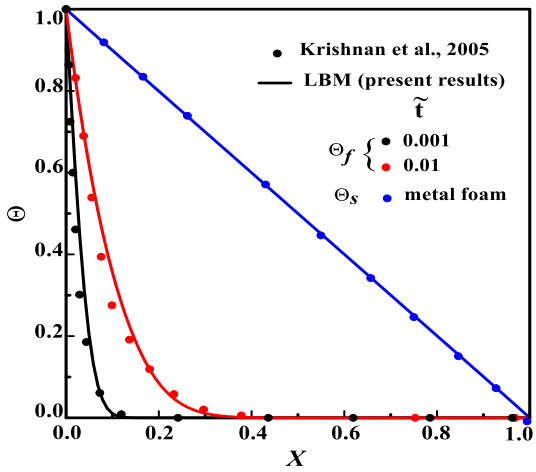

Fig. 7. Dimensionless fluid and solid temperature evolution (Θ_f, Θ_s) vs. dimensionless transverse distance X at $Y = 0.5$ for a nil interstitial Nusselt ($Nu_i = 0$) and $Da = 10^{-2}, Pr = 50, Ra = 10^6, Ste = 1$.

In addition, it should be pointed out that further validity of the approach and code used in this study has already been confirmed in a recently published article [45].

5. Results and discussion

It is worth recalling that the laminar flow through a rectangular open-ended channel filled with a porous media and a PCM, is the main concern of this work. Unless up-stated, all computations reported in this study were performed with a uniform grid composed of 480x120, after having conducting the grid sensitivity to demonstrate the solution independence with respect to the grid. To control the computation time and cost, The SRT-TLBM, associated with the enthalpy method, is applied to perform REV-scale simulations of charging/discharging, in which the forcing term is related to the medium's porosity (see relationships (26) and (28)).

The effect of two parameters that are *Re* (200 and 400) and porosity ($\varepsilon = 0.5, 0.7$ and 0.9) are presented and commented in this section while keeping fixe the numbers of Prandtl, Biot, Stephan, Eckert, thermal conductivity ratio ($Pr = 50, Bi = 0.1, Ste = 1, Kr = 10^{+3}, Rc = 1, Ec = 5$).

First, the LTNE assumption is secured using the following criterion [29, 31]:

$$LTNE = \sum_N \left| \Theta_s - \Theta_f \right| / N \tag{48}$$

$N = 480x120$ being the total number of nodes in the computation domain.

It should be noted that it is well accepted that the LTE condition is valid if this criterion is less than 5% and conversely, the LTNE condition is secured if it is greater than 5%. Such a criterion allows to exhibit the LTNE spatial distribution (or LTE) through the channel. In other words, it delineates the channel zones where the LTNE occurs. These areas can also be

revealed by considering the (Bi , Kr) chart (not shown herein). So, based on this idea, simulations are performed to show that the LTNE condition exceeds or not 5% for the charge and discharge processes for Re = 200 and 400, and at the porosity range considered here, viz. $0.5 \le \varepsilon \le 0.9$. Fig. 8 shows the results of Re's effect set by the porosity during the charging and discharging processes. It is clear that the LTNE is secured (LTNE > 5%) in the selected parameters range. It turns out that it increases when Re and ε increase corroborating that there is no thermal equilibrium between the two phases.

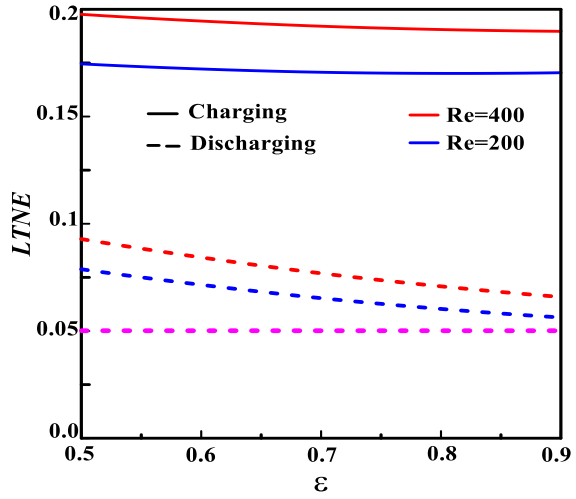

Fig. 8. LTNE parameter during charging and discharging vs. ε parameterized by Re, and at $Pr = 50, Bi = 0.1, Ste = 1, Kr = 10^{+3}, Ec = 5, Rc = 1$. Also plotted in the figure is the LTNE's minimum value (5%) commonly accepted (the horizontal dotted line).

The medium's porosity effect on the U-velocity at the two Re numbers considered, during the charging and discharging processes is depicted in Fig. 9. From this figure, it appears that the velocity profiles approach each other regardless of the metal foam porosity. In other word, it can be seen that the hot fluid velocity is very slightly affected by the decrease in porosity. This involves that the solid phase paraffin, filling pores and acting as an obstacle, slows down the dispersion of the hot fluid flow. In contrast, during the discharge period, the flow velocity raises with Re and drops with ε. Indeed, the cold fluid flow moves more easily through the pores due to the viscous forces reduction.

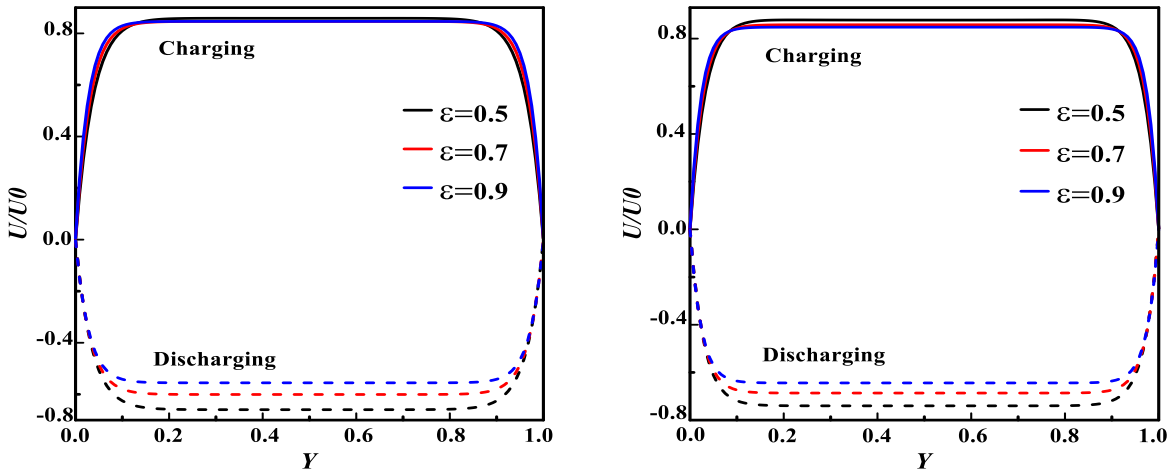

(a) Re = 200 **(b) Re = 400**

Fig. 9. Porosity effect on U-velocity during charging and discharging processes for two *Re* numbers at X = 0.5 with $Pr = 50, Bi = 0.1, Ste = 1, Kr = 10^{+3}, Ec = 5, Rc = 1$.

During charging and discharging processes, the LTNE intensity $(\Theta_f - \Theta_s)$ is depicted vs. the streamwise coordinate for the porosities considered here and two *Re* values (200, 400), while keeping the other parameters fixed. During the charging process and for *Re* = 200, the increasing curves almost coincide with each other, then decrease regardless of the porosity (Fig. 10a). It turned out that, beyond $X \approx 1.8$, these curves decrease when ε increases. Noted the existence of a X_c-critical value where a local maximum is exhibited which depends on *Re* number and porosity. For Fig. 10b and ever in the charging case and for *Re* = 400, the curves exhibit the same behavior up to a critical X_c of order of 1.5. There is a significant rise due to the forced convection improvement at low porosity, confirming a prevailing heat convective transfer. During the discharge process, and from the exit region, $(\Theta_f - \Theta_s)$ is strongly affected by the porosity and is slightly dependent on *Re*. It slightly increases through the entire channel to reach a local maximum near the entrance region.

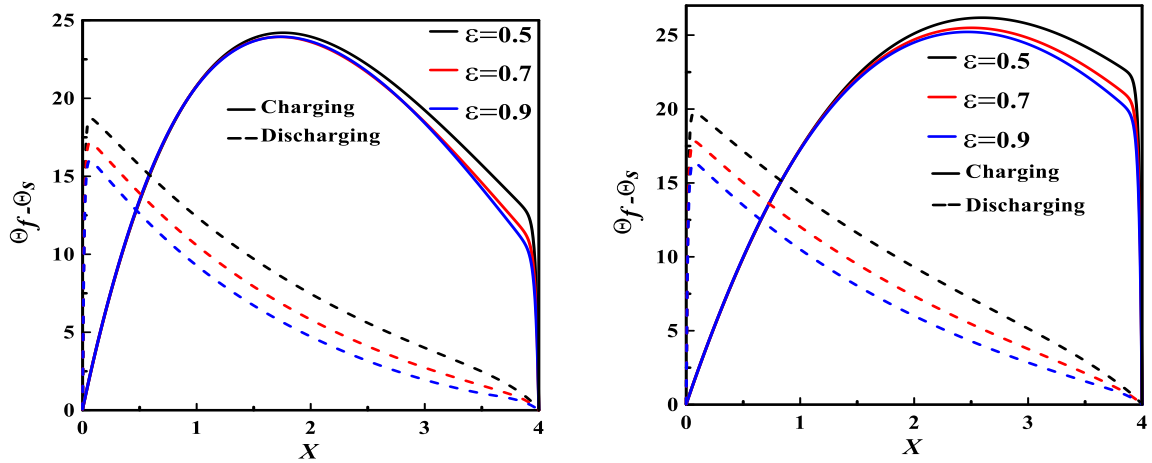

(a) Re = 200 **(b) Re = 400**

Fig. 10. Porosity effect on LTNE intensity ($\Theta_f - \Theta_s$) during charging and discharging processes for two *Re* numbers at Y=0.5 with $Pr = 50, Bi = 0.1, Ste = 1, Kr = 10^{+3}, Ec = 5, Rc = 1$.

Fig. 11 provides the porosity effect on the irreversibility in the system expressed by the dimensionless entropy generation rate (*Ns*). For both processes, it can be seen that the *Re* increase gives rise to that of the *Ns*, while the porosity decrease enhance it. During the charging process and for *Re* = 200, the *Ns*'s profiles remain almost the same beyond the channel middle whatever the porosity, reach a maximum, then decrease quite sharply. Note that, for the case *Re* = 400, *Ns* is larger, while generally setting out the same behavior. By neatly examining such a figure, it turns out that this figure shows that the porosity reduction improves the entropy generation rate (*Ns*) due to viscous effects dominance which accentuate irreversibility. Compared to the first process, during the second (the discharging), the *Ns*'s amplitude is lower (up to at least 4 times), while remaining strongly affected by the porosity because of the fluid dispersion under viscous effects. To sum up, the two processes degrade the PCM, which prejudices its suitability for the mission sought.

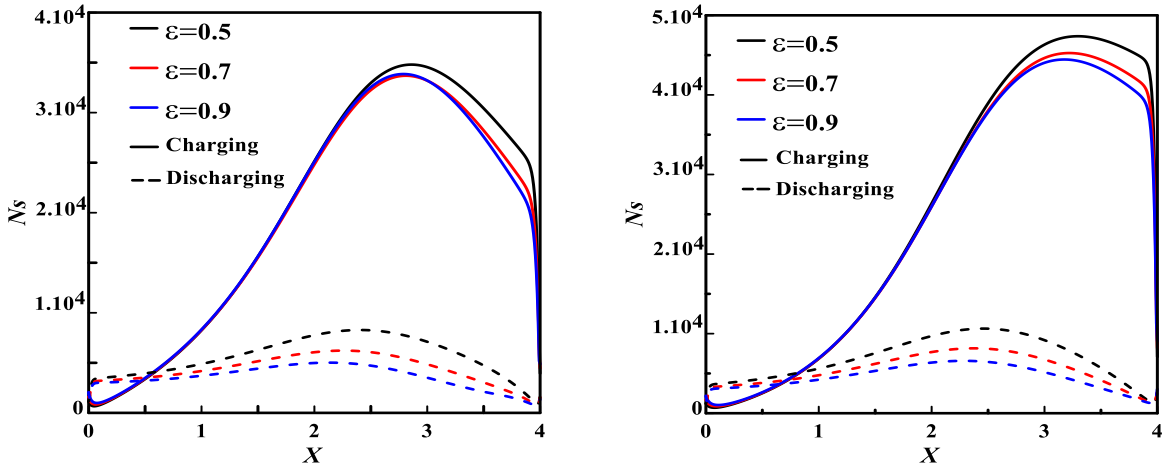

(a) Re=200 **(b) Re=400**

Fig. 11. Porosity effect on the entropy generation rate (*Ns*) during charging and discharging processes for two *Re* numbers at Y = 0.5 with $Pr = 50, Bi = 0.1, Ste = 1, Kr = 10^{+3}, Ec = 5, Rc = 1$.

The porosity effect on the average entropy generation rate (Ns_{av}) during the two processes is presented through the Fig. 12 set by *Re*. During the two processes, it decreases slightly for the two *Re* values regarded. As seen, such a parameter increases with *Re* whatever the process. During the second process, the *Ns*'s amplitude is lower (up to at least 3 to 4 times) for *Re* = 200 and 400, respectively compared to the first process, corroborating both the heat transfer irreversibility and the PCM degradation. So, it can be stated that irreversibilities in all the system are more accented with small porosities, the thermal conductivity ratio (*Kr*) between the fluid and solid phases being high, which promotes the heat transferred.

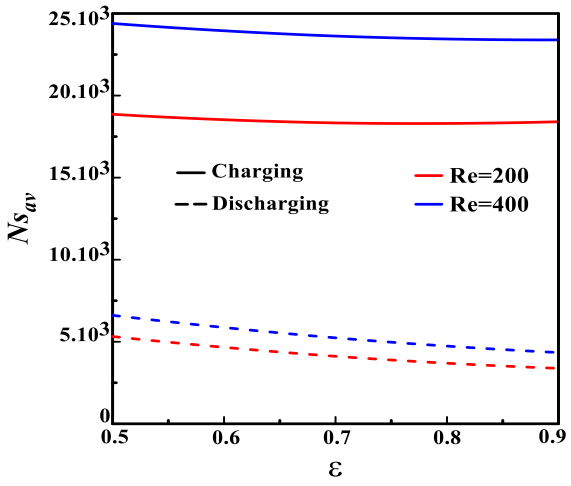

Fig. 12. Porosity effect on the average entropy generation rate (Ns_{av}) during charging and discharging processes for two *Re* numbers with $Pr=50, Bi=0.1, Ste=1, Kr=10^{+3}, Ec=5, Rc=1$.

The effect porosity on the Bejan number (*Be*) during the charging and discharging process at $Y=0.5$ is reported in Fig. 13. During both processes, in the near vicinity of the channel entrance and exit, *Be* is less than 0.5 indicating that FFI dominates the overall system irreversibility. Elsewhere, *Be* exceeds the prescribed threshold, viz 0.5 for *Re* = 200 and 400 regardless the porosity value, and exhibits a plateau (an asymptotic value) almost all along the channel, except at its entry and exit. In addition, the porosity has little influence on *Be* during the first process. However, it manifests itself slightly during the second process in the areas far from the entry and exit where the HTI's dominance prevails. Note that this distribution highlights critical areas (close to entry and exit) where HTF and HTI have identical contributions.

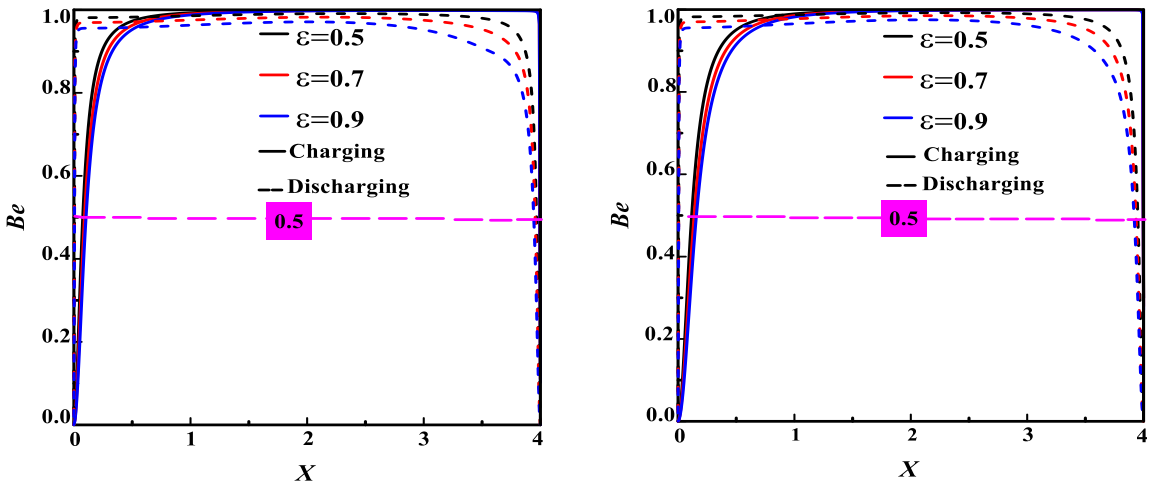

(a) Re=200 **(b) Re=400**

Fig. 13. Porosity effect on the Bejan number (*Be*) during charging and discharging processes for two Reynolds numbers at Y = 0.5 with $Pr=50, Bi=0.1, Ste=1, Kr=10^{+3}, Ec=5, Rc=1$.

The effect of *Re* on the average *Be* number vs. porosity during charging and discharging processes is shown on Fig. 14. It is worth noting that, at low Re and porosity values, the HTI's contribution is further pronounced whatever the key parameters regarded.

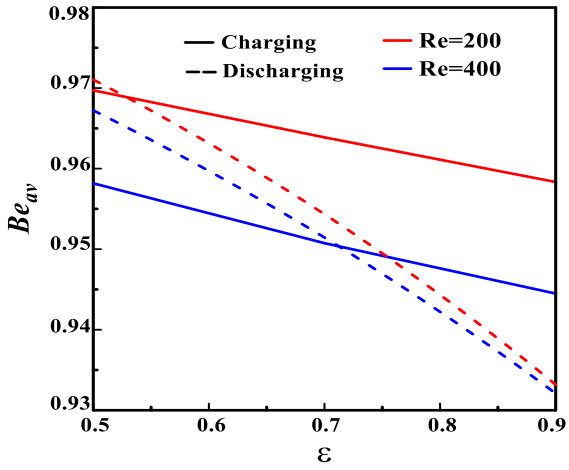

Fig. 14. Porosity effect on the average Bejan number (Be_{av}) during charging and discharging processes for two Reynolds numbers with $Pr=50, Bi=0.1, Ste=1, Ec=5, Kr=10^{+3}, Rc=1$.

The panels in Figs. 15 and 16 show the melt front time evolvement in the porous channel as the porosity increases from 0.5 to 0.9 (left to right) for *Re* = 200 and 400, respectively. The red and blue zones indicate the melted and no-melted PCM, while the other colors show the PCM mushy zone. For the lowest *Re* (Fig. 15), it is found that, over time, the more the porosity increases, the more the melt front advances forward while accelerating ($\varepsilon=0.7$) or slowing ($\varepsilon=0.9$) the melting. Explicitly, for $\varepsilon=0.5$, the melting process takes place promptly (in a short time) compared to cases of $\varepsilon=0.7$ and $\varepsilon=0.9$. Thereby, it appears that decreasing the porosity promotes the melting due to the heat transfer diffusion downstream of the channel, the heat in pores being intensified.

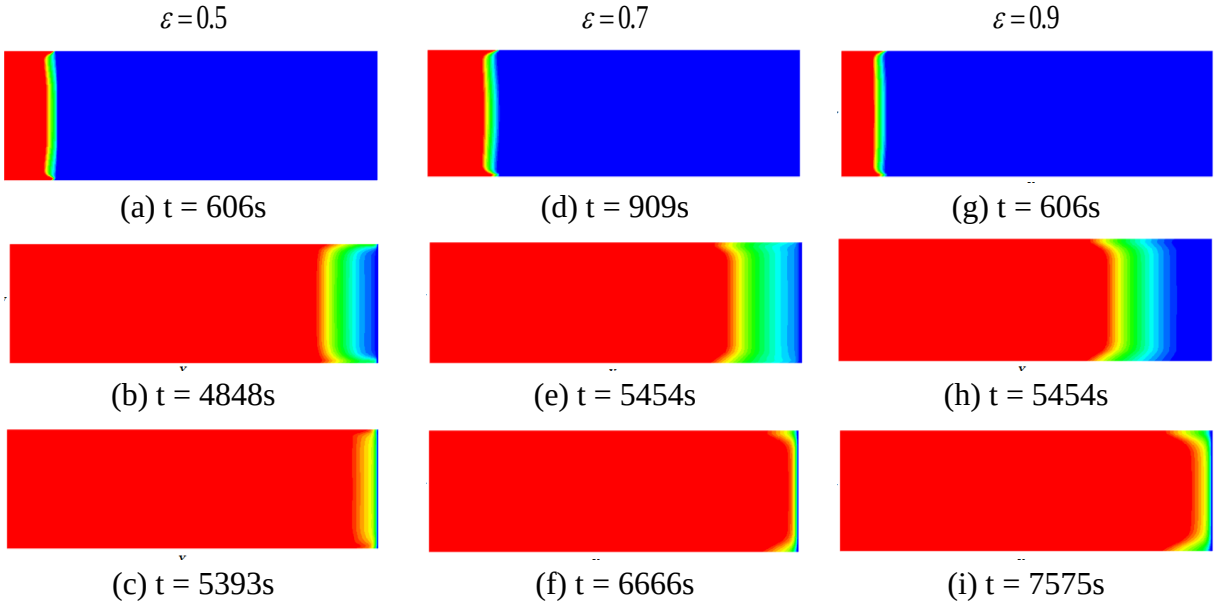

Fig. 15. Porosity effect on Melt front (Γ) at various times during charging process for *Re* = 200 with $Pr = 50, Bi = 0.1, Ste = 1, Ec = 5, Kr = 10^{+3}, Rc = 1$.

The profiles of the Melt front (Γ) in the porous channel for Re = 400 can be observed in Fig. 16 for a quantitative comparison. These contours reflect both the melt front shape and its time-evolvement when varying the Reynolds number. Qualitatively speaking, the case corresponding to the highest *Re* (Fig. 16) is similar to the previous case. Nevertheless, the regular evolution of the melting front is manifest as the porosity passes from 0.5 to 0.9. To sum up, the Re increase promotes the melting, while the skeleton porosity speed up its velocity due to the heat transfer dominating that mitigates the viscous effects in pores.

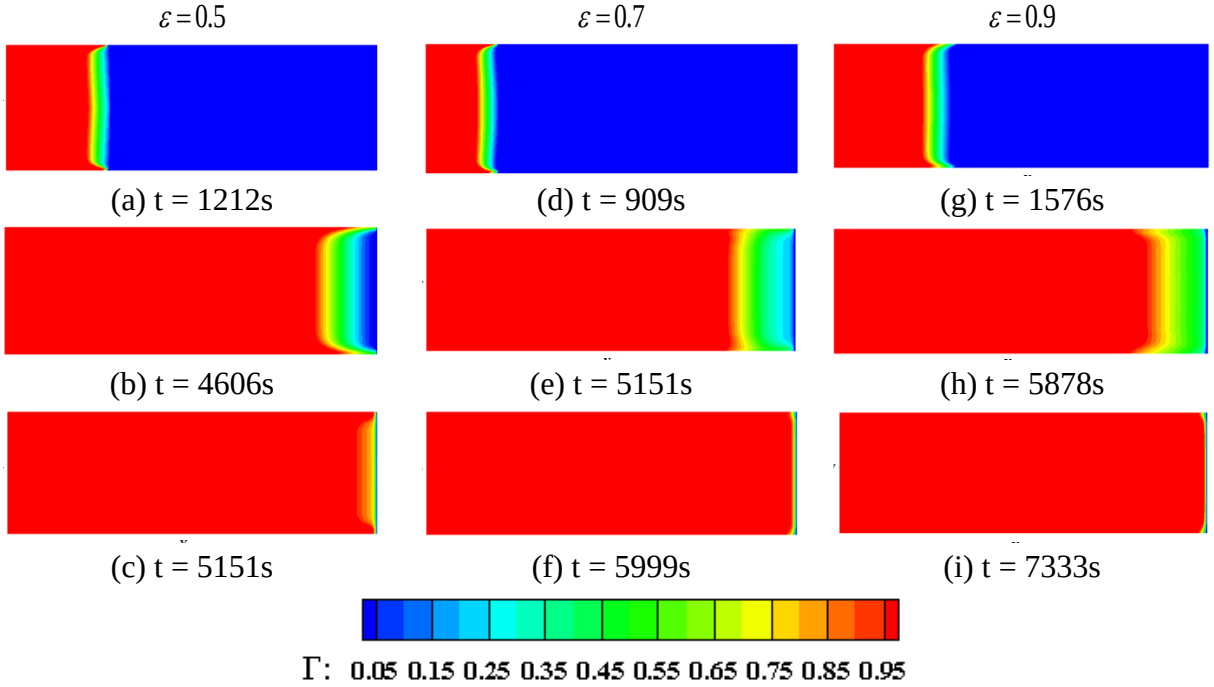

Fig. 16. Porosity effect on Melt front (Γ) at various times during charging process for *Re* = 400 with $Pr = 50, Bi = 0.1, Ste = 1, Ec = 5, Kr = 10^{+3}, Rc = 1$.

6. Conclusion

The present numerical study investigated the porosity effect on heat transfer under unsteady forced convection in an open-ended horizontal channel filled with a porous structure and a PCM. The simulations have been achieved using the SRT-TLBM method to which is added the enthalpy method. Validations of the TLBM code with relevant previous studies have shown good agreement. To cope with the present study under non local thermal equilibrium condition, the REV-scale TLBM has been applied with three density functions for dynamic and thermal fields of PCM and solid foam. The relevance of the porosity effect is highlighted and commented during the charging (melting) and discharging (solidifying) processes. In the

study context, the results presented here allow to deepen our knowledge of the porosity effect on the heat transfer rate and the evolution of the melting front.

Based on the numerical results obtained, the following outcomes can be stated as:

- The LTNE condition prevails during the charging and discharging processes regardless the parameters considered.
- Small porosities' use speeds up the PCM melting rate.
- The smaller the porosity, the more the *Re* increase improves the thermal convection between the two phases (solid/fluid) and the higher the LTNE intensity is.
- Irreversibility during the cycle (charging/discharging) can be mitigated using high porosity materials.
- The cycle is faster with low porosity metal foam due to the high thermal conductivity ratio.

Such conclusions hold for the Reynolds range dealt herein.

Besides, it turned out that the thermal lattice Boltzmann method is an approach that can handle unsteady forced convective fusion problems in a porous rectangular duct with phase change.

Conflict of interest

The authors declare that they have no known competing financial interests or personal relationships that could have influenced the work reported in this paper. Besides, they state no conflict of interests regarding authorship and/or publication of this manuscript.

Acknowledgements

The authors would like to thank Prof. A. JEMNI, Head of LESTE/ENIM/Univ. Monastir, Tunisia for useful discussions which helped to better design this paper.

Conflict of interest

The authors declare that they have no known competing financial interests or personal relationships that could have influenced the work reported in this paper.

CRediT authors statement

Riheb Mabrouk: Methodology, Software, Validation, Investigation, Writing-original draft; **Hassane Naji**: Conceptualization, Methodology, Investigation, Formal analysis, Supervision, Writing - Reviewing and Editing; **Hacen Dhahri:** Conceptualization, Methodology, Investigation, Formal analysis, Writing - Reviewing and Editing, Project administration, Supervision; **Sihem Hammouda:** Investigation, Resources, Validation, Visualization; **Zohir Younsi:** Formal analysis, Investigation, Validation, Visualization.

References

[1] P. Zhang, X. Xiao, Z. W. Ma, A review of the composite phase change materials: fabrication, characterization, mathematical modeling and application to performance enhancement, Appl. Energy 165 (2016) 472-510. https://doi.org/10.1016/j.apenergy.2015.12.043.

[2] P. Y. Huo, Y. Guo, Z. Rao, Investigation on the thermal performance of phase change material/porous medium-based battery thermal management in pore scale, Int. J. Energy Research 43 (2019) 767-778. https://doi.org/10.1002/er.4307.

[3] Z. Wang, Z. Zhang, L. Jia, L. Yang, Paraffin and paraffin/aluminum foam composite phase change material heat storage experimental study based on thermal management of lion battery, Appl. Therm. Eng. 78 (2015) 428-436. https://doi.org/10.1016/j.applthermaleng.2015.01.009.

[4] Y. Huo, Z. Rao, Lattice Boltzmann investigation on phase change of nanoparticle-enhanced phase change material in a cavity with separate plate, Energ. Conver. Manage. 154 (2017) 420-429. https://doi.org/10.1016/j.enconman.2017.11.039.

[5] Y. Lv, W. Situ, X. Yang, G. Zhang, Z. Wang, A novel nanosilica-enhanced phase change material with anti-leakage and anti-volume-changes properties for battery thermal management, Energ. Conver. Manage. 163 (2018) 250-259. https://doi.org/10.1016/j.enconman.2018.02.061.

[6] D. Y. Lee, K. Vafai, Analytical characterization and conceptual assessment of solid and fluid temperature differentials in porous media, Int. J. Heat Mass Transf. 42 (1999) 423-435. https://doi.org/10.1016/S0017-9310(98)00185-9.

[7] H. Xu, L. Gong, Sh. Huang, M. Xu, Flow and heat transfer characteristics of nanofluid flowing through metal foams, Int. J. Heat Mass Transf. 83 (2015) 399-407. https://doi.org/10.1016/j.ijheatmasstransfer.2014.12.024.

[8] K. Vafai, Handbook of Porous Media, CRC Press, Taylor & Francis Group, Boca Raton, FL 33487, 2005.

[9] D.A. Nield, A. Bejan, Convection in Porous Media, 4th ed., Springer-Verlag, New York, USA, 2013.

[10] H. J. Xu, Z.G. Qu, W.Q. Tao, Thermal transport analysis in parallel-plate channel filled with open-celled metallic foams, Int. Commun. Heat Mass Transf. 38 (7) (2011) 868-873. https://doi.org/10.1016/j.icheatmasstransfer.2011.04.015.

[11] O. Mesalhy, K. Lafdi, A. Elgafy, K. Bowman, Numerical study for enhancing the thermal conductivity of phase change material (PCM) storage using high thermal conductivity porous matrix, Energy Convers. Manage. 46 (2005) 847-867. https://doi.org/10.1016/j.enconman.2004.06.010.

[12] J. L. Yang, L.J. Yang, C. Xu, X. Z. Du, Numerical analysis on thermal behavior of solid-liquid phase change within copper foam with varying porosity, Int. J. Heat Mass Transf. 84 (2015) 1008-1018. https://doi.org/10.1016/j.ijheatmasstransfer.2015.01.088.

[13] S. Chen, G. D. Doolen, Lattice Boltzmann method for fluid flows, Annu. Rev. Fluid Mech. 30 (1998) 329-64. https://doi.org/10.1146/annurev.fluid.30.1.329.

[14] C. K. Aidun, J. R. Clausen, Lattice-Boltzmann method for complex flows, Annu. Rev. Fluid Mech. 42 (2010) 439-72. https://doi.org/10.1146/annurev-fluid-121108-145519.

[15] T. Krüger, H. Kusumaatmaja, A. Kuzmin, O. Shardt, G. Silva , E. M. Viggen, The Lattice Boltzmann Method, Principles and Practice, Springer International Publishing, 2017. https://doi.org/10.1007/978-3-319-44649-3.

[16] Q. Li, K. H. Luo, Q. J. Kang, Y. L. He, Q. Chen, Q. Liu, Lattice Boltzmann methods for multiphase flow and phase-change heat transfer, Prog. Energy Combust. Sci. 52 (2016) 62-105. https://doi.org/10.1016/j.pecs.2015.10.001.

[17] Y. B. Tao, Y. You, Y. L. He, Lattice Boltzmann simulation on phase change heat transfer in metal foams/ paraffin composite phase change material, Appl. Therm. Eng. 93 (2016) 476-485. https://doi.org/10.1016/j.applthermaleng.2015.10.016.

[18] W. S. Jiaung, J. R. Ho, C. P. Kuo, Lattice Boltzmann method for the heat conduction problem with phase change, Numer. Heat Transf. B 39 (2001) 167-187. https://doi.org/10.1080/10407790150503495.

[19] Y. L. He, Q. Liu, Q. Li, W.Q. Tao, Lattice Boltzmann methods for single-phase and solid-liquid phase-change heat transfer in porous media: A review, Int. J. Heat Mass Transf. 129 (2019) 160-197. https://doi.org/10.1016/j.ijheatmasstransfer.2018.08.135.

[20] D. Gao, Z. Chen, D. Zhang, L. Chen, Lattice Boltzmann modeling of melting of phase change materials in porous media with conducting fins, Appl. Therm. Eng. 118 (2017) 315-327. https://doi.org/10.1016/j.applthermaleng.2017.03.002.

[21] Z. Chen, D. Gao, J. Shi, Experimental and numerical study on melting of phase change materials in metal foams at pore scale, Int. J. Heat Mass Transf. 72 (2014) 646-655. https://doi.org/10.1016/j.ijheatmasstransfer.2014.01.003.

[22] D. Gao, F. B. Tian, Zh. Chen, D. Zhang, An improved lattice Boltzmann method for solid-liquid phase change in porous media under local thermal non-equilibrium conditions,

Int. J. Heat Mass Transf. 110 (2017) 58-62. https://doi.org/10.1016/j.ijheatmasstransfer.2017.03.014.

[23] G.F. Al-Sumaily, M.C. Thompson, Forced convection from a circular cylinder in pulsating flow with and without the presence of porous media, Int. J. Heat Mass Transf. 61 (2013) 226-244. https://doi.org/10.1016/j.ijheatmasstransfer.2013.01.067.

[24] D. Gao, Z. Chen, L. Chen, A thermal lattice Boltzmann model for natural convection in porous media under local thermal non-equilibrium conditions, Int. J. Heat Mass Transf. 70 (2014) 979-989. https://doi.org/10.1016/j.ijheatmasstransfer.2013.11.050.

[25] V. Joshi, M. K. Rathod, Constructal enhancement of thermal transport in metal foam-PCM composite-assisted latent heat thermal energy storage system, Numer. Heat Transf. A 75(6) (2019) 413-433. https://doi.org/10.1080/10407782.2019.1599270.

[26] W. Zhao, D. France, Wenhua Yu, T. Kim, D. Singh, Phase change material with graphite foam for applications in high-temperature latent heat storage systems of concentrated solar power plants, Renew. Energy 69 (2014) 134-146. https://doi.org/10.1016/j.renene.2014.03.031.

[27] R. Rabhi, B. Amami, H. Dhahri, A. Mhimid, Entropy generation for an axisymmetric MHD flow under thermal non-equilibrium in porous micro duct using a Modified Lattice Boltzmann Method, J. Magn. Magn Mater. 419 (2016) 521-532. https://doi.org/10.1016/j.jmmm.2016.06.068.

[28] G.F. Al-Sumaily, A. Nakayama, J. Sheridan, M.C. Thompson, The effect of porous media particle size on forced convection from a circular cylinder without assuming local thermal equilibrium between phases, Int. J. Heat Mass Transf. 55 (2012) 3366-3378. https://doi.org/10.1016/j.ijheatmasstransfer.2012.03.007.

[29] G. F. Al-Sumaily, J. Sheridan, M. C. Thompson, Validation of thermal equilibrium assumption in forced convection steady and pulsatile flows over a cylinder embedded in a porous channel, Int. Commun. Heat Mass Transf. 43 (2013) 30-38. https://doi.org/10.1016/j.icheatmasstransfer.2013.01.009.

[30] M. Torabi, N. Karimi, G.P. Peterson, S. Yee, Challenges and progress on the modelling of entropy generation in porous media: A review, Int. J. Heat Mass Transf. 114 (2017) 31-46. https://doi.org/10.1016/j.ijheatmasstransfer.2017.06.021.

[31] A. Abdedou, K. Bouhadef, R. Bennacer, Forced convection in a self-heating porous channel: local thermal non-equilibrium model, Thermal Science 21 (2017) 2413-2423. https://doi.org/10.2298/TSCI150201110.

[32] O. A. López-Núñez, J. A. Alfaro-Ayala, O. A. Jaramillo, J. J. Ramírez-Minguela, J. Carlos Castro, C. E. Damian-Ascencio, S. Cano-Andrade, A numerical analysis of the energy

and entropy generation rate in a Linear Fresnel Reflector using computational fluid dynamics, Renew. Energy 146 (2020) 1083-1100. https://doi.org/10.1016/j.renene.2019.06.144.

[33] C. Pan, L.S. Luo, C.T. Miller, An evaluation of lattice Boltzmann schemes for porous medium flow simulation, Comput. Fluids 35 (2006) 898-909. https://doi.org/10.1016/j.compfluid.2005.03.008.

[34] D. Gao, F.B. Tian, Zh. Chen, D. Zhang, An improved lattice Boltzmann method for solid-liquid phase change in porous media under local thermal non-equilibrium conditions, Int. J. Heat Mass Transf. 110 (2017) 58-62. https://doi.org/10.1016/j.ijheatmasstransfer.2017.03.014.

[35] A. Yehya, H. Naji, L. Zalewski, Experimental and numerical characterization of an impure phase change material using a thermal lattice Boltzmann method, Appl. Therm. Eng. 154 (2019) 738-750. https://doi.org/10.1016/j.applthermaleng.2019.03.026.

[36] B. Amami, H. Dhahri, A. Mhimid, Viscous dissipation effects on heat transfer, energy storage and entropy generation for fluid flow in porous channel submitted to uniform magnetic field, J. Transp. Porous Media 17 (2014) 841-859., https://doi.org 10.1615/JPorMedia.v17.i10.10.

[37] Z. Guo, Ch. Zheng, B. Shi, Thermal lattice Boltzmann equation for low Mach number flows: Decoupling model, Phys. Rev. E 75 (2007) 036704. https://doi.org/10.1103/PhysRevE.75.036704.

[38] Y. Shi, T. S. Zhao, Z. L. Guo, Thermal lattice Bhatnagar-Gross-Krook model for flows with viscous heat dissipation in the incompressible limit, Phys. Rev. E 70 (2004) 066310. https://doi.org/10.1103/PhysRevE.70.066310.

[39] Q. Zou, and X. He, On pressure and velocity boundary conditions for the lattice Boltzmann BGK model, Phys. Fluids 6 (1997) 1591-1598. https://doi.org/10.1063/1.869307.

[40] S. Biswas, P. Sharma, B. Mondal & G. Biswas, Analysis of Mixed Convective Heat Transfer in a Ribbed Channel Using the Lattice Boltzmann Method, Numer. Heat Tr. A Appl. 68 (2015) 75-98. https://doi.org/10.1080/10407782.2014.965095.

[41] C. S. Kumar, S. Mohankumar, M. Geier, A. Pattamatta, Numerical investigations on convective heat transfer enhancement in jet impingement due to the presence of porous media using Cascaded Lattice Boltzmann method, Int. J. Therm. Sci. 122 (2017) 201-217. http://dx.doi.org/10.1016/j.ijthermalsci.2017.08.020.

[42] M. Jourabian, A. A. R. Darzi, D. Toghraie, Melting process in porous media around two hot cylinders: Numerical study using the lattice Boltzmann method, Physica A 509 (2018) 316-335. https://doi.org/10.1016/j.physa.2018.06.011.

[43] S. Y. Kim, B. H. Kang, J. M. Hyun, Heat transfer from pulsating flow in a channel filled with porous media, Int. J. Heat Mass Transf. 37 (1994) 2025-2033. https://doi.org/10.1016/0017-9310(94)90304-2.

[44] S. Krishnan, J.Y. Murthy, S.V. Garimella, A two-temperature model for solid-liquid phase change in metal foams, J. Heat Transf. 127 (2005) 995-1004. https://doi.org/10.1115/1.2010494.

[45] R. Mabrouk, H. Dhahri, H. Naji, S. Hammouda, Z. Younsi, Lattice Boltzmann simulation of forced convection melting of a composite phase change material with heat dissipation through an open-ended channel, Int. J. Heat Mass Transf. 153 (2020) 119606. https://doi.org/10.1016/j.ijheatmasstransfer.2020.119606.